

Bayesian connective field modeling using a Markov Chain Monte Carlo approach



Azzurra Invernizzi^{a,b,e,*}, Koen V. Haak^d, Joana C. Carvalho^c, Remco J. Renken^b,
 Frans W. Cornelissen^{a,b}

^a Laboratory for Experimental Ophthalmology, University of Groningen, University Medical Center Groningen, Groningen, the Netherlands

^b Cognitive Neuroscience Center, Department of Biomedical Sciences of Cells & Systems, University Medical Center Groningen, Groningen, the Netherlands

^c Laboratory of Preclinical MRI, Champalimaud Centre for the Unknown, Lisbon, Portugal

^d Donders Institute for Brain Cognition and Behaviour, Radboud University Medical Center, Nijmegen, the Netherlands

^e Department of Environmental Medicine and Public Health, Icahn School of Medicine at Mount Sinai, New York, NY, USA

ARTICLE INFO

Keywords:

Connective field modelling
 Bayesian modelling
 Markov chain Monte Carlo
 population receptive field
 Visual cortex, Cortical circuitry

ABSTRACT

The majority of neurons in the human brain process signals from neurons elsewhere in the brain.

Connective Field (CF) modelling is a biologically-grounded method to describe this essential aspect of the brain's circuitry. It allows characterizing the response of a population of neurons in terms of the activity in another part of the brain. CF modelling translates the concept of the receptive field (RF) into the domain of connectivity by assessing, at the voxel level, the spatial dependency between signals in distinct cortical visual field areas. Thus, the approach enables to characterize the functional cortical circuitry of the human cortex. While already very useful, the present CF modelling approach has some intrinsic limitations due to the fact that it only estimates the model's explained variance and not the probability distribution associated with the estimated parameters. If we could resolve this, CF modelling would lend itself much better for statistical comparisons at the level of single voxels and individuals. This is important when trying to gain a detailed understanding of the neurobiology and pathophysiology of the visual cortex, notably in rare cases. To enable this, we present a Bayesian approach to CF modeling (bCF). Using a Markov Chain Monte Carlo (MCMC) procedure, it estimates the posterior probability distribution underlying the CF parameters. Based on this, bCF quantifies, at the voxel level, the uncertainty associated with each parameter estimate. This information can be used in various ways to increase confidence in the CF model predictions. We applied bCF to BOLD responses recorded in the early human visual cortex using 3T fMRI. We estimated both the CF parameters and their associated uncertainties and show they are only weakly correlated. Moreover, we show how bCF facilitates the use of effect size (beta) as a data-driven parameter that can be used to select the most reliable voxels for further analysis. Finally, to further illustrate the functionality gained by bCF, we apply it to perform a voxel-level comparison of a single, circular symmetric, Gaussian versus a Difference-of-Gaussian model. We conclude that our bCF framework provides a comprehensive tool to study human functional cortical circuitry in health and disease.

1. Introduction

In recent years, functional magnetic resonance imaging (fMRI) in combination with biologically-motivated computational models of receptive fields has become a popular technique for researchers aiming to advance our understanding of the human visual system (Wandell and Wade, 2003; Park et al., 2002; Meindertsma et al., 2017; Dumoulin and Wandell, 2008; Zeidman et al., 2018; Adaszewski et al., 2018; Benson and Winawer, 2018; Wandell and Winawer, 2015). While modeling receptive fields in the visual cortex in terms of their response

to visual stimuli has its merits, it is known that the majority of the neurons in the human brain process and integrate signals from neurons that are located elsewhere in the brain (Robinson, 1989). The resulting spatial and temporal integration, to which we will refer as cortico-cortical interactions, support key brain functions such as perception and attention. However, exactly how these interactions are shaped by the cortical circuitry that functionally connects different cortical areas, remains unclear.

One possible approach to describe the cortical circuitry underlying such cortico-cortical interactions is connective field (CF) modelling

* Corresponding author at: Laboratory for Experimental Ophthalmology, University Medical Center Groningen, P.O.Box 30.001, 9700 RB Groningen, the Netherlands.

E-mail addresses: a.invernizzi@umcg.nl, azzurra.invernizzi@mssm.edu (A. Invernizzi).

(Haak et al., 2013). CF modeling allows characterizing the cortical response properties of a population of neurons in terms of the activity in another region of the visual cortex. In essence, it translates the concept of the stimulus-referred receptive field (RF) into the domain of connectivity by assessing the spatial dependency between signals in distinct cortical visual field areas (Haak et al., 2013). This neural-referred RF is also known as the cortico-cortical population RF (cc-pRF). The CF approach can be used to assess the spatial integration properties of the visual system from either task-evoked or resting-state neural responses (Gravel et al., 2014; Bock et al., 2015). So far, it has been mainly used to study connective plasticity in various ophthalmic and neurological diseases (Haak et al., 2013; Halbertsma et al., 2019; Haak et al., 2016; Ahmadi et al., 2019; Carvalho et al., 2019; De Best et al., 2019).

The standard CF (sCF) approach has some intrinsic properties which limit its use in a variety of potential applications. These limitations are due to the fact that the optimal model fit is obtained by minimizing the difference between the prediction and measured signal on the basis of minimizing the residual sum of squares (RSS). Consequently, model comparison is only possible based on the percentage of explained variance of the model and there is no information to quantify the variability and reliability of the various estimated CF parameters. If we could retrieve the latter type of information, CF modelling would lend itself much better for statistical comparisons at the level of single individuals, which can be important in the context of patient studies, e.g. with a neurodegenerative disorder, such as glaucoma. This would be essential when assessing rare cases, where group averages are not available. Moreover, it would become possible to evaluate the probability distribution of CF models at the level of single voxels. This may help to unravel the detailed neurobiology of the visual cortex by testing alternative models to explain task or resting-state related responses (e.g. comparing different receptive field shapes while taking model complexity into account).

The present limitations of the CF modeling approach may be overcome by determining the full underlying probability distributions for the various CF parameters. From these, we can quantify, at the voxel level, the uncertainty associated with each parameter estimate. Theoretically, uncertainty is a useful evaluation parameter by itself. First of all, it can establish confidence in the CF model predictions. Secondly, it may be valuable for investigating and meaningfully explaining differences within parameter distributions as a result of different conditions, tasks, interventions or pathology. Finally, it may be used to identify model biases that, for example, result from over- or under-fitting or a co-dependence of parameters. Removing such dependencies may help to further improve the CF model predictions.

To enable this new functionality, we present a Bayesian inference framework for CF modelling, which we will refer to with bCF. Using a Markov Chain Monte Carlo (MCMC) procedure (Robert and Casella, 2011), bCF provides the underlying posterior probability distribution of the CF parameters (position and size in case of the most basic model). From this distribution, we can derive the uncertainty associated with each of these parameters. In addition, we also retain the effect size of the CF model, which we will refer to as beta (adhering to the nomenclature used by Zeidman et al. (2018)). We show how beta can be used as a data-driven threshold. To further illustrate the functionality gained by bCF we show that, at the voxel level, single Gaussian (SG) models are favoured over Difference-of-Gaussian (DoG) models.

2. Methods

2.1. Participants

Twelve healthy female participants (mean age 22 years, s.d. = 1.8 years) with normal or corrected-to-normal vision and without a history of neurological disease were included. Previously, these data have been used as a normative dataset in work that did not use our present framework (Halbertsma et al., 2019). Anonymized and prepro-

cessed time series for each visual area can be downloaded at this link: <http://www.visualneuroscience.nl/cf>.

The ethics board of the University Medical Center Groningen (UMCG) approved the study protocol. All participants provided written informed consent. The study followed the tenets of the Declaration of Helsinki.

2.2. Stimuli presentation and description

The visual stimuli were displayed on a MR compatible screen located at the head-end of the MRI scanner with a viewing distance of 118 cm. The participants viewed the complete screen through a mirror placed at 11 cm from the eyes and supported by the 32-channel SENSE head coil. Screen size was 36×23 ° of visual angle and the distance from the participant's eyes to the screen was approximately 75 cm. Stimuli were generated and displayed using the Psychtoolbox (<http://psychtoolbox.org/>) and VISTADISP toolbox (VISTA Lab, Stanford University), which are both MatLab based (Brainard, 1997; Pelli, 1997). The stimulus consisted of drifting bar apertures (of 10.2° radius) with a high contrast checkerboard texture on a grey (mean luminance) background. A sequence of eight different bar apertures with four different bar orientations (horizontal, vertical and diagonal orientations), two opposite motion directions and four periods of mean-luminance presentations comprised the stimulus presentation that lasted 192 s. To maintain stable fixation, participants were instructed to focus on a small colored dot present in the center of the screen and press a button as soon as the dot changed color. The complete visual field mapping paradigm was presented to the participant six times, with a new scan started for each repetition.

2.3. Data acquisition

MRI and fMRI data were obtained using a 3T Philips Intera MRI scanner (Philips, the Netherlands), with a 32-channel head coil. For each participant, a high-resolution T1-weighted three-dimensional structural scan was acquired (TR = 9.00 ms, TE = 3.5 ms, flip-angle = 8, acquisition matrix = $251 \times 251 \times 170$ mm, field of view = $256 \times 170 \times 232$, voxel size = $1 \times 1 \times 1$ mm). Six visual field map (VFM) functional T2^{*}-weighted, 2D echo planar images were obtained (voxel resolution of $2.5 \times 2.5 \times 2.5$, field of view = $190 \times 190 \times 50$ mm, TR = 1500 ms, TE = 30 ms). Each VFM scan lasted for 192 s with a total of 136 volumes. A short T1-weighted anatomical scan with the same field of view chosen for the functional scans was acquired and used in the co-registration step between functional and anatomical volume.

2.4. Standard fMRI data analysis

Preprocessing and standard (pRF and CF) analyses of fMRI data were done using ITKGray (<http://www.itk.org>) and the mrVista toolbox for MatLab (VISTASOFT, <https://github.com/vistalab/vistasoft>; <http://www.white.stanford.edu>). The same steps and parameters have been used in previous studies (Haak et al., 2013; Dumoulin and Wandell, 2008) and also applied to this dataset (Halbertsma et al., 2019; Invernizzi et al., 2021).

The Bayesian CF approach and Bayesian CF model comparison were developed and performed using MatLab 2016b (The Mathworks Inc., Natick, Massachusetts).

2.4.1. Preprocessing

For each participant, the structural scan was reoriented and aligned in a common space defined using the anterior commissure-posterior commissure line (AC-PC line) as reference. Next, grey and white matter were automatically segmented using Freesurfer, and manually adjusted using ITKGray in order to minimize possible segmentation errors.

All functional data were pre-processed and analyzed using the mrVista toolbox. First, head motion within and between scans were corrected by using multiresolution alignment of MRI brain volumes

(Nestares and Heeger, 2000). Then, functional data were aligned using an in-house code based on the following steps: 1) run FLIRT (the automated registration tool of FLS, <https://fsl.fmrib.ox.ac.uk/fsl/fslwiki>, Woolrich et al., 2009; Smith et al., 2004; “FSL”, 2012), then 2) run the robust registration algorithm described by Nestares et al. and finally 3), manually check the obtained aligned with rxAlign in MrVista. Lastly, a trilinear interpolation of the temporal time series extracted from the functional data onto the volumetric segmented anatomical grey and white matter obtained using the ITKGray/Freesurfer. In this way, the functional time series will be spatially interpolated to the nearest functional voxel (VISTASOFT, <https://github.com/vistalab/vistasoft>; <http://www.white.stanford.edu>).

2.4.2. Population Receptive Field (pRF) mapping

Retinotopy scans were analyzed using a model-based analysis, known as the population receptive field (pRF) method (Dumoulin and Wandell, 2008), which enables delineating the visual field maps of interest. Based on the best fitting prediction obtained using a 2D Gaussian model, the hemodynamic response (HRF), and the stimulus aperture, we estimate the visual field mapping parameters (eccentricity, polar angle and pRF size). The best model fit was projected onto a smoothed 3D mesh of the cortex, on which the visual areas were functionally identified using standard techniques (Wandell and Winawer, 2015; Sereno et al., 1994; Engel et al., 1997).

Based on the phase reversals in the pRF maps, visual cortical areas (V1, V2, V3, hV4, LO1 and LO2) were located and manually delineated for each individual participant according to standard criteria (Dumoulin and Wandell, 2008; Amano et al., 2009; Brewer et al., 2005; Dougherty et al., 2003; Harvey and Dumoulin, 2011; Wandell, 2011; Wandell et al., 2007; Winawer et al., 2010; Zuiderbaan et al., 2012) and by using a probabilistic atlas of the human visual cortex (Wang et al., 2015) as guidance for higher visual order areas (hV4, LO1 and LO2). Note that the foveal confluence (which would be $<\sim 1.5$ deg eccentricity) is part of the source areas as it is typically harder to distinguish between visual areas (Schira et al., 2009). These areas were then used to define the target and the source regions for the CF analysis.

2.4.3. Standard connective field modelling

In short, in the standard CF approach (Haak et al., 2013), the optimal CF model parameters are estimated in order to explain an observed signal of a single voxel in a target region (e.g. V2 or V3) based on the signals in a source region (e.g. V1). To do so, a 2D Gaussian CF model (with parameters position and size) integrates over the BOLD time series of the voxels in the source region in order to calculate a predicted time series. The optimal fit of the model is determined by minimizing the difference between the predicted and observed time series of the target voxel (by minimizing the residual sum of squares (RSS)). The center of the CF is restricted to a voxel location in the source region. For each voxel in the target region, the parameter values that result in an optimal model fit are estimated and retained.

2.4.4. Visualizing connective field model parameters

For visualization purposes and qualitative analyses, the CF model parameters obtained for each voxel can be projected onto a smoothed 3D mesh of the cortical surface. The CF position on the cortex can be converted from cortical units (in mm) into visual field map units (eccentricity, polar angle; in degrees of visual angle). This was done via a weighted integration of the visual field map properties, estimated via pRF mapping (Section 2.4.2), of the voxels encompassed by the CF in the source region.

2.5. Bayesian connective field modelling

As in the standard approach, Bayesian CF modelling tries to explain the observed signal of a voxel in a target region based on the signals in a source region. However, rather than estimating only the optimal

parameters, the Bayesian approach estimates the full underlying posterior probability distribution associated with each CF parameter. This can be achieved by extensive and iterative sampling of the parameter space of the model, which is done here using a Markov Chain Monte Carlo (MCMC) procedure. The parameter space of the model is spanned by the following parameters: the CF center (location on a mesh grid that contains the location of all the voxels of the source area), the CF size, and the CF effect size (which scales the amplitude of the predicted to that of the observed signal). At each MCMC iteration, new values for the parameters are proposed and compared to that of the current one. Depending on the outcome of this comparison, the proposed model parameters are accepted or not. The rejected values for the model parameters are neither stored nor used for estimating the CF parameters. For each target voxel, a total of 17,500 iterations are run, of which the first 10% are discarded to allow for burn-in (Liu et al., 2016; Chib 2011). It is our experience that this number of MCMC draws provides a reasonable balance between accuracy and computational time for this data set. An example using a selected number of target voxels in V2 for two participants is presented in Supplementary Material (Table T1) for the interested reader. The posterior distributions are estimated based on the samples of the remaining iterations. Throughout, we will use the abbreviation bCF to indicate the Bayesian CF approach. The code for the bCF framework can be obtained via <http://www.visualneuroscience.nl/cf>. The next sections describe the model (2.5.1), the two parameter estimation options for the MCMC procedure (2.5.2), the CF model parameters, the latent variables, and their priors (2.5.3). We will follow the nomenclature of (Zeidman et al., 2018). An overview of the bCF approach is presented in Fig. 1.

2.5.1. Model definition

The CF model generates a predicted time series $p(t)$ to explain an observed time series $y(t)$ of a target voxel (Eq. 1). To generate $p(t)$, a CF $g(v)$ is convolved with the observed time series of the voxels (v) in a source $a(v, t)$ (with a representing the neuronal population input based on the BOLD signal change ($\Delta\%$) (Eq. 2). The CF $g(v)$ is, in its most elementary form, a 2D circular symmetric Gaussian with a width sigma (σ) (Eq. 3).

$$y(t) = p(t)\beta + \epsilon \quad (1)$$

$$p(t) = \sum_v [a(v, t)*g(v)] \quad (2)$$

$$g(v) = \exp - \left[D(v, v_0)^2 / 2\sigma^2 \right] \quad (3)$$

In Eq. 1, β defines the effect size and ϵ is the error term. In Eq. 3, the Gaussian CF $g(v)$ is defined in terms of distance along the cortical surface. Therefore, for all the voxels (v) in the source, the distance matrix $D(v, v_0)$ contains their shortest distances to the CF center (v_0) along a triangular mesh representation of this cortical surface manifold. In order to remain consistent with the standard CF model implemented by Haak et al, these distances are computed using Dijkstra's algorithm (Dijkstra, 1959). Note that $g(v)$ is scaled to ensure that the total area under the gaussian surface, as calculated across the entire source region, is equal to one.

2.5.2. The bCF approach has two parameter estimation options

Both parameter estimation options provide valid CF parameter and uncertainty estimates and will be described in the next two sections. The first bCF option (A) estimates the standard CF parameters (position and size) using a Bayesian model. In this option the effect size (β , scaling the amplitude of the predictor to the amplitude of the measured signal) is estimated using ordinary least squares fit (OLS) but it is not retained. The second bCF option (B) estimated under joint estimation the β parameter together with the other bCF parameters. In this last option, β is retained as meaningful and worth analyzing further. Therefore,

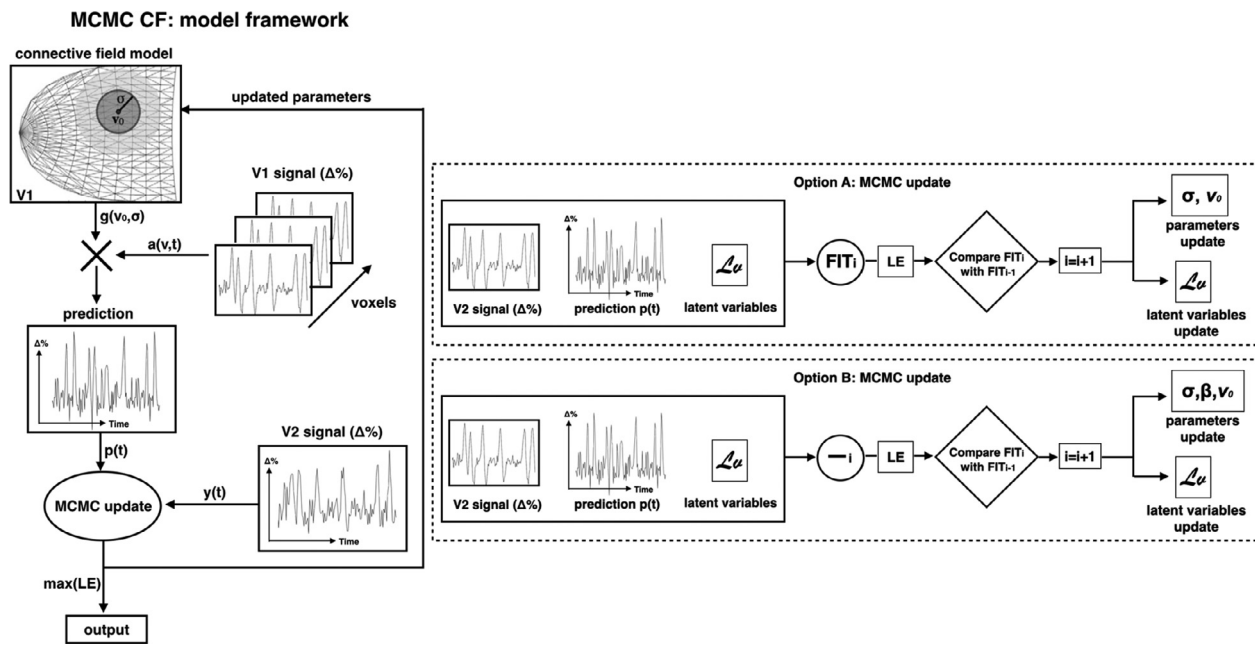


Fig. 1. Overview of the Bayesian CF framework. In this example, we use the bCF approach to estimate the V1▶V2 connective field (i.e. we estimate the source region in V1 of a V2 target voxel). Following the CF definition of Haak et al. (2013), the predicted time series $p(t)$ is obtained by the overlap between a 2D symmetric Gaussian $g(v)$ and the neuronal population inputs $a(v, t)$, which are the fMRI times series of all the voxels in the source region (in this case V1). In the MCMC procedure, the predicted time series $p(t)$, the observed time series of the (in this case V2) target voxel $y(t)$ and the latent variables (L_v) are used to define and estimate the CF parameters. Based on the maximum likelihood associated with the error (MLE) calculated between $p(t)$ and $y(t)$, the latent variables (L_v) are updated for use in the next iteration. Two different MCMC update options are provided: in option A, the likelihood estimation is obtained after scaling $p(t)$ using an ordinary least squares fit (OLS) method thereby estimating the effect size (indicated by FIT in the Fig.). In option B, the amplitude/scaling parameter (β) is jointly estimated with the other CF parameters and retained for further analyses - the fitting procedure used in this option is indicated by ($-i$). Figure adapted from Haak et al. (2013).

the primary difference between bCF options is in how effect size is estimated and used. The user can select their preferred option based on the research question posed. To aid the reader, pseudocode for the MCMC procedure can be found in the Supplementary Materials (paragraph S2).

2.5.2.1. Parameter estimation option A. This option, referred to as bCF_A, closely replicates the standard CF approach and is computationally relatively ‘light weight’. At each iteration, the CF parameters (σ, β) are estimated as follows. First, a predicted signal $p(t)$ is generated for CF position (v_0 proposed) according to Eq. 2. Secondly, per time point, the error e_t between $p(t)$ and the measured signal $y(t)$ is calculated using an ordinary least squares fit (OLS) with free parameter β . Then, the log-likelihood L_t associated with e_t is estimated (Eq. 4). We assume that e_t follows a standard normal density function: $N(0,1)$. After estimating the mean and standard deviation of e ($\hat{\mu}_e$ and $\hat{\sigma}_e$), we calculate a maximum likelihood estimate (MLE). In this option, only the prior for σ (I_σ ; Section 2.5.3) is used in calculating MLE (Eq. 5). Effect size β is not retained.

$$L_t = \log(N(e_t, \hat{\mu}_e, \hat{\sigma}_e)) \quad (4)$$

$$MLE_A = \sum_t L_t + \log(N(I_\sigma, 0, 1)) \quad (5)$$

Next, the MLE of the proposed parameter values ($MLE_{proposed}$) is compared to that of the previously accepted values ($MLE_{accepted}$) based on an Acceptance ratio score Ar (6).

$$Ar = e^{MLE_{proposed} - MLE_{accepted}} \quad (6)$$

Ar will be >1 if $MLE_{proposed}$ is greater than $MLE_{accepted}$, and the proposal will be accepted. If $MLE_{accepted}$ is greater than

$MLE_{proposed}$, Ar will be between 0 and 1 and the proposal will be accepted with probability Ar . Then, the next MCMC iteration takes place.

2.5.2.2. Parameter estimation option B. This option, referred to as bCF_B, primarily differs from bCF_A in that at each iteration, the MCMC procedure jointly estimates the CF parameters σ and β . Secondly, the priors for both σ and β (I_σ, I_β ; Section 2.5.3) are used in calculating the MLE (Eq. 7). Finally, β is retained for use in further analyses and thresholding (see paragraph 2.6.2).

$$MLE_B = \sum_t L_t + \log(N(I_\sigma, 0, 1)) + \log(N(I_\beta, -2, 5)) \quad (7)$$

2.5.3. Proposing parameters using latent variables and priors

As already described in Section 2.5.2, at each iteration of the MCMC procedure, new values for the parameters of the CF model are proposed (referred to below with *proposed*) and, depending on the outcome of the Ar evaluation (Eq. 6), accepted (referred to below with *accepted*) or rejected. In this section, we describe how the proposed values are generated. Following Zeidman et al., initial values, priors, and latent variables have been selected (for more details, please see Zeidman et al., 2018). We use latent variables and corresponding transfer functions to relate these to the actual CF parameters. In order to obtain a likelihood on a model, it is beneficial to have (latent) variables, e.g. I_σ , follow a gaussian distribution on the interval $-\infty$ and $+\infty$ (Eqs. 5 and 7, Table 1). At the same time, the transfer function can constrain the CF parameters to reflect prior knowledge. The latent variables (L_v) are presented in Table 1.

2.5.3.1. Connective field position. At each iteration, a new CF position (v_0 proposed) is selected that is at a distance $step$ from the currently accepted CF center (v_0 accepted). This distance $step$ ranges between 0 and

Table 1

Latent variables definitions. Rows list the latent variables used in the two bCF estimation options for both the single Gaussian (SG) and Difference of Gaussian (DoG) models (see Sections 2.5.1 and 2.5.4). Latent variables are used for the following reason: in order to obtain a likelihood on a model, it is beneficial to have (latent) parameters, e.g. I_σ , following a gaussian distribution. At the same time, the CF parameters are constrained. For example σ is bound to be between 0 and 10 mm. The transformation from latent to non-latent variable allows us to go from the latent variable defined on the interval $-\infty$ and $+\infty$ distribution to the CF variable with compact support.

Latent variables (L_v)		
Bayesian CF model	SG	DoG
Option A	$I_s I_\sigma$	$I_s I_\sigma I_{\sigma_2}$
Option B	$I_s I_\sigma I_\beta$	$I_s I_\sigma I_\beta I_{\sigma_2} I_{\beta_2}$

a maximum possible stepsize [0 ms] Eqs. 8 and (9). The maximum step size (ms) is defined as half the maximum distance in the matrix $D(v, v_0)$ (Eq. 8). To calculate $step$, a latent variable I_s is randomly drawn from a normal distribution $N(0,1)$ and multiplied with maximum step size (ms), resulting in a flat prior for step size. The newly proposed CF position (v_0 proposed) is set to the voxel in the source region with a distance to the current position that is as close as possible to $step$. If multiple positions are found, one of these is selected at random.

$$ms = \max(D(v, v_0 \text{ accepted})) / 2 \quad (8)$$

$$step = ms * NCDF(I_s, 0, 1) \quad (9)$$

Note that on the first iteration, the CF center (v_0 accepted) is set at the position of a random voxel in the source region. Based on the proposed and accepted CF centers respectively, two distance matrices d_{proposed} (Eq. 10) and d_{accepted} (Eq. 11) are derived.

$$d_{\text{proposed}} = D(v, v_0 \text{ proposed}) \quad (10)$$

$$d_{\text{accepted}} = D(v, v_0 \text{ accepted}) \quad (11)$$

2.5.3.2. Connective field size. Simultaneous with a newly proposed sample position, also a new CF size (σ) is proposed. For σ , its associated latent variable is I_σ . The prior for I_σ is defined by a normal distribution $N(0, 1)$ (Eq. 12).

$$\sigma = (r - r_0) * NCDF(I_\sigma, 0, 1) + r_0 \quad (12)$$

$NCDF$ denotes the normal cumulative distribution function. Note that σ is constrained to the range $[r_0, r]$, where r_0 is the minimum radius and r is the maximum radius for the CF (which are set to 0.01° and 10.5° , respectively). Note that r_0 can be set to any arbitrarily small non-zero number.

At each MCMC iteration, an I_σ proposed is drawn from a normal probability density function N centered around the current value with a width of w (Eq. 13). Note that w has a fixed value of 2.

$$I_\sigma \text{ proposed} = N(I_\sigma \text{ accepted}, w) \quad (13)$$

2.5.3.3. Effect size. In the bCF_B, (Section 2.5.2.2), β is estimated jointly with CF size and constrained to be positive (Zeidman et al., 2018) using the following equation:

$$\beta = \exp(I_\beta) \quad (14)$$

The latent variable I_β is defined with a prior distribution $N(-2, 5)$ and the proposed β value is controlled by I_β proposed (Eq. 15).

$$I_\beta \text{ proposed} = N(I_\beta, w) \quad (15)$$

The initial values of I_σ initial, I_β initial and w are set to 1, -5 and 2, respectively. As an aside, note that in bCF_A (Section 2.5.2.1), β is esti-

mated at a higher hierarchical level inside the loop using an OLS fit and can, theoretically, range between $-\infty$ and $+\infty$.

2.5.4. Alternative kernel: difference of Gaussians

In addition to the single Gaussian (SG) model described above, we also implemented a Difference of Gaussian (DoG) model. The DoG model has previously been proposed for modeling surround suppression in stimulus-driven pRF models Zeidman et al., 2018; Zuiderbaan et al., 2012). As for the SG model, the initial values, prior and latent variables for the DoG model have been selected following (Zeidman et al., 2018; Zuiderbaan et al., 2012). In the DoG model, the first Gaussian represents the center and is defined using the same parameters as in the SG model (i.e. v_0 , σ_1 , and β_1). The second Gaussian of the DoG represents the surround suppression and uses the same position parameter as the SG, but is defined using independent parameters for size (σ_2) and amplitude (β_2). Size parameter σ_2 is constrained to be equal to or larger than σ_1 (Eq. 16). The amplitude β_2 is constrained to be negative and smaller than β_1 (Eqs. 17 and 18). This is enforced using two scaling parameters σ_d and β_d , for size and amplitude, respectively.

$$\sigma_2 = \sigma_1 + \sigma_d \quad (16)$$

$$\beta_2 = \max(\beta_1 - \beta_d, 0) \quad (17)$$

$$P_{\text{DoG}}(t) = p_1(t)\beta_1 - p_2(t)\beta_2 \quad (18)$$

Parameter σ_d is constrained to be between $[0, r_d]$ (see Eq. 12) using a latent variable I_{σ_2} which is defined according to a standard normal distribution $N(0,1)$ (see Eq. 13). r_d is the largest allowed difference in radius for the second Gaussian compared to the first and is set to 0.5° . This means that the initial value of σ_2 can be between 0 and 0.5° deg larger than that of σ_1 . The β_d was forced to be positive (Zeidman et al., 2018) with a latent variable I_{β_2} with a prior distribution $N(-2, 5)$ (see Eq. 15).

In this study, when estimating the DoG model, we used bCF_B in which all β_1 and β_2 values and their associated probabilities are retained for further analysis. The initial values of $I_{\sigma_2 \text{ initial}}$ and $I_{\beta_2 \text{ initial}}$ were set to 5 and 10, respectively. The DoG implementation for bCF_A is described in the supplementary material.

2.5.5. Model validation and comparison

For each participant, the sCF and both bCF V1 served as the source region that is sampled by various target regions (V2, V3, hV4, LO1 and LO2), as in (Baseler et al., 2011; Haak et al., 2013; Haak et al., 2012; Winawer et al., 2010). Target and source regions were defined as described in Section 2.4.2. Note that the results of several CF are represented in stimulus space/world coordinates based on the pRF properties of the center voxel in the source region (V1). These pRF properties were defined per participant (see Methods, 2.4.2).

When validating the output of the sCF and bCF_A models, we thresholded on variance explained (Haak et al., 2013). In those cases, only voxels for which the best-fitting CF model explained at least 15% of the time-series variance were included. This particular threshold level was chosen to be consistent with previous literature (Baseler et al., 2011; Haak et al., 2013; Haak et al., 2012; Winawer et al., 2010). The thresholding approach applied in bCF_B is described below in Section 2.6.2. To quantify the level of agreement between the sCF and either of the bCF options, the estimates for the CF parameters (position and size) for each target region are compared using Pearson correlations at both the participant and the group level. Correlation values higher than 0.5 and p-values below 0.05 were considered statistically significant. Furthermore, a family-wise error corrected (FWE) permutation test was used to determine whether differences based on the Variance Explained (VE) parameter between SG and DoG models were significant. The permuted

labels were repeated 1000 times per subject, $p \leq 0.05$ was considered statistically significant.

2.6. Bayesian analysis and new model features

2.6.1. Uncertainty

Based on a quantile analysis of the estimated posterior distribution, we computed a voxel-wise uncertainty measure (Papadopoulos and Yenung, 2001) for the bCF parameters estimates as follows:

$$U = Q_3 - Q_1 \quad (17)$$

where Q_3 and Q_1 represent the upper and lower quantiles of the posterior distribution, respectively. Furthermore, we computed the cross-correlation coefficients to quantify possible dependencies between the bCF parameters (VE, sigma and beta; the latter only for bCF_B) and their associated uncertainties. For each target region, these correlations were computed at both the participant and the group level.

2.6.2. Beta thresholding

In fMRI research, it is generally considered good practice to limit analysis of the parameter estimates to voxels with reliable model fits. In the pRF literature, this is commonly done by setting a variance explained threshold (typically fixed at 15%). Another approach would be to verify whether the probability of an estimated model effect size is larger than may be expected on the basis of chance alone. As such, the estimated values must be compared against their null-distribution. Often, this null-distribution can be derived from theoretical considerations (e.g. t-distributions) and estimates of the degrees of freedom of the model (parametric approach). However, due to both spatial and temporal dependencies in the data, it is generally preferred to construct an empirical null-distribution by sampling the model estimations using randomly generated data with a spatiotemporal covariance structure that is similar to that of the real data (non-parametric approach).

In this context, a second consideration pertains to the statistic upon which thresholding will be based. Intuitively, the overall model fit is quantified by the total amount of variance that is explained by the model. The threshold criterion can then be chosen such that this quantity is significantly greater than zero (e.g. the quantity falls within the 95th percentile of the null distribution). When the model involves just a single free scaling parameter (i.e. effect size), testing whether this scaling is greater than zero is often equivalent to testing the significance of the overall model fit (i.e. variance explained). This is the case in standard pRF and CF modelling as well as in bCF_A . There, a candidate model prediction is iteratively generated and the goodness of fit is determined using a single scaling parameter (Eq. 1). However, in bCF_B , the scaling parameter beta is jointly estimated with sigma. Thresholding by testing whether beta is greater than zero may therefore yield different results compared to thresholding based on variance explained. This is due to potential dependencies between beta and sigma. In the case of a joint estimation, the parameter beta can be interpreted as a form of response gain (summarizing the combined effects of the neuronal and BOLD response gains). Therefore, in bCF_B , testing the significance of beta provides an alternative for thresholding. This more directly addresses the question of whether or not the activity of a voxel in the target region is meaningfully associated with that in the source region.

In order to use beta as a data-driven threshold, a proxy distribution for the null hypothesis (which states that there is no correlation between the source and target region) is required. We calculate this null distribution based on surrogate BOLD time series. To do so, for each voxel in the target region, surrogate BOLD time series were generated from its actual BOLD time series using the iterative Amplitude Adjusted Fourier Transform method (iAAFT; Räth and Monetti, 2009; Schreiber and Schmitz, 1996). Using this method, the temporal correlations between source and target were removed while preserving the

spatial relationships between voxels within the source region. Then, the bCF_B model is fitted to the surrogate time series of the target voxel and the real BOLD time series of the source region. Using the betas estimated based on the surrogate time series, we have implemented two variants: 1) a beta-uncorrected threshold and 2) a beta-corrected threshold. Fig. 2 provides an overview of both. The beta-uncorrected threshold is determined independently for each voxel in the target region. The bCF_B model is fitted to a total of 40 surrogate time series generated for the voxel (this number was chosen for computational feasibility). In this case, the null distribution is the aggregate of all the betas estimated at voxel level. The voxel-specific beta-uncorrected threshold is obtained by calculating the 95th percentile of this null distribution. In case of the beta-corrected threshold, the posterior null distribution is the aggregate of the betas estimated for all voxels in the target region. The beta-threshold is the 95th percentile of this aggregated null distribution. In this way, the beta-threshold is familywise error (FWE) corrected for all the voxels in the target region. While in regular use a single aggregate distribution will be sufficient, in the present study, we generated 40 aggregate null distributions for the target region. These were used to verify the appropriateness of the beta-corrected threshold variant. One of these distributions was selected at random and used to determine the beta threshold.

2.6.3. Model selection

To compare the SG and DoG models, three parameters were considered: the variance explained (VE) of the model, the Bayesian Information Criterion (BIC, see Eq. 18; Schwarz, 1978; Myung and Pitt, 2004) and Akaike's Information Criterion (AIC, Eq. 19).

$$BIC = \ln(n)*k - 2*\ln(MLE) \quad (18)$$

$$AIC = 2*k - 2*\ln(MLE) \quad (19)$$

Where n is the number of data points in a time series (in our study set to 124) and k is the number of free model parameters (set to 2 and 4 for the SG and DoG models, respectively). Per target voxel, the best model was determined based on having either the lowest BIC value. For completeness, we also show how the model can be determined based on the lowest AIC value and the highest VE.

3. Results

To preview our results, we observed a good level of agreement between the sCF and the bCF models. We estimated the uncertainty and (in)dependence of the bCF parameters (σ and β). Moreover, we determined the effect of thresholding based on the model's effect size. Finally, we found that a CF model based on a single Gaussian was preferred over one based on a DoG to explain the observed BOLD correlations between visual areas.

3.1. Standard and bCF models provide similar CF estimates

Fig. 3 shows the bCF_A and the sCF estimates plotted on a smoothed 3D cortical surface of a representative participant. The maps were obtained using V1 as the source and V2, V3, hV4, LO1 and LO2 as the target regions. The maps for both methods show a clear visuotopic organization for all the CF parameters estimated and are in good agreement (Fig. 3, panels a and b). Furthermore, Fig. 4 illustrates a generally good level of correlation between the sCF and the bCF_A model estimates at the voxel level for this participant. For sake of completeness, retinotopy maps and correlation plots for all participants are reported in Supplementary Material (Figs. S4 and S5). Specifically, panels a and b indicate that the coverage of the visual field is similar between the two methods. Furthermore, panel c indicates that the same is true for the CF size. Note that some exceptions are found (e.g. eccentricity in LO2, CF size in hV4).

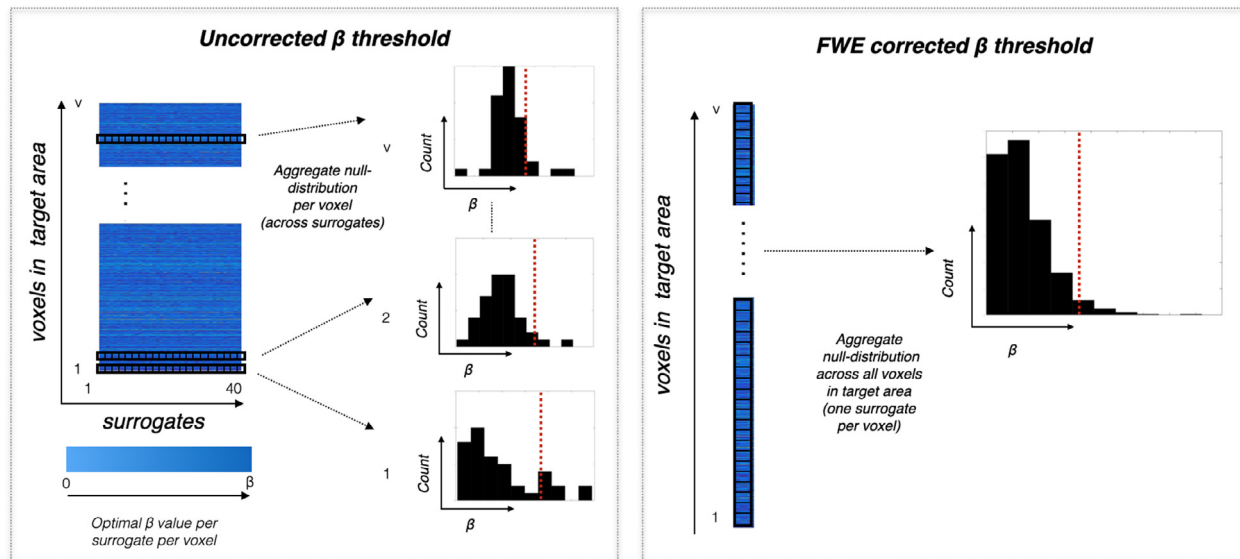


Fig. 2. Illustration of the two beta thresholding options available during Bayesian CF modeling. For each voxel in the target region, a null distribution for beta is estimated based on surrogate BOLD time series. The resulting optimal fits for a sample of 40 voxels are presented in the voxel-by-surrogate matrix (left hand side). The bCF_B has two options for thresholding based on beta. Left: when selecting the “uncorrected threshold” option, an optimal threshold for beta is computed for each individual voxel in the target region. The beta-threshold is based on the 95th percentile of the null distribution for that particular voxel (indicated by the red line in each of the histograms). Consequently, the optimal beta-threshold will be specific to each voxel. Right: when selecting the “FWE-corrected threshold” option, the optimal beta-threshold is based on the 95th percentile of the aggregate null distributions of all voxels in the target region.

Table 2

Group level (median) correlations between visual field map parameters derived from pRF, standard CF and both Bayesian CF models. Correlation coefficients indicate the level of agreement in the eccentricity (*rho*, Spearman’s correlations) and polar angle (*theta*, circular correlations) maps for the standard CF and both Bayesian CF models with the ones directly derived by pRF mapping (gold standard). Correlation and p-values were first estimated at the participant level and then concatenated across all participants to determine the median and interquartile range (IQR). The correlation values for each participant are reported in the Supplementary Materials (Tables T3 and T4).

Eccentricity												
ROIs	Standard CF				bCFa				bCFb			
	<i>rho</i>	<i>IQR[Q₁]</i>	<i>IQR[Q₃]</i>	<i>p-value</i>	<i>rho</i>	<i>IQR[Q₁]</i>	<i>IQR[Q₃]</i>	<i>p-value</i>	<i>rho</i>	<i>IQR[Q₁]</i>	<i>IQR[Q₃]</i>	<i>p-value</i>
V1 > V2	0.868	0.822	0.905	<i>p</i> < 0.001	0.865	0.819	0.905	<i>p</i> < 0.001	0.873	0.814	0.899	<i>p</i> < 0.001
V1 > V3	0.825	0.783	0.874	<i>p</i> < 0.001	0.824	0.775	0.873	<i>p</i> < 0.001	0.822	0.763	0.865	<i>p</i> < 0.001
V1 > hV4	0.809	0.731	0.838	<i>p</i> < 0.001	0.791	0.731	0.837	<i>p</i> < 0.001	0.788	0.711	0.839	<i>p</i> < 0.001
V1 > LO1	0.781	0.724	0.816	<i>p</i> < 0.001	0.781	0.717	0.819	<i>p</i> < 0.001	0.791	0.721	0.823	<i>p</i> < 0.001
V1 > LO2	0.705	0.595	0.816	0.002	0.656	0.538	0.759	0.004	0.662	0.462	0.731	0.001
Polar Angle												
ROIs	Standard CF				bCFa				bCFb			
	<i>rho</i>	<i>IQR[Q₁]</i>	<i>IQR[Q₃]</i>	<i>p-value</i>	<i>rho</i>	<i>IQR[Q₁]</i>	<i>IQR[Q₃]</i>	<i>p-value</i>	<i>rho</i>	<i>IQR[Q₁]</i>	<i>IQR[Q₃]</i>	<i>p-value</i>
V1 > V2	0.917	0.844	0.929	<i>p</i> < 0.001	0.918	0.870	0.929	<i>p</i> < 0.001	0.914	0.854	0.936	<i>p</i> < 0.001
V1 > V3	0.834	0.744	0.916	<i>p</i> < 0.001	0.843	0.703	0.916	<i>p</i> < 0.001	0.854	0.713	0.927	<i>p</i> < 0.001
V1 > hV4	0.799	0.524	0.921	<i>p</i> < 0.001	0.796	0.513	0.918	<i>p</i> < 0.001	0.832	0.497	0.921	<i>p</i> < 0.001
V1 > LO1	0.812	0.554	0.902	<i>p</i> < 0.001	0.826	0.553	0.901	<i>p</i> < 0.001	0.810	0.567	0.896	<i>p</i> < 0.001
V1 > LO2	0.723	0.515	0.833	0.003	0.675	0.512	0.817	0.001	0.649	0.426	0.842	0.003

Table 2 lists the group-level correlations for the eccentricity and polar angle maps reconstructed on the basis of the sCF and both bCF model outputs with those derived directly using pRF mapping (which serves as the gold standard).

Overall, we observed good levels of agreement between the outputs of the sCF and bCF frameworks. This indicates that bCF accurately estimates the cortico-cortical properties of the human visual cortex. Correlation values obtained at the single participant level are reported in the supplementary material (Table T3 and T4). Additionally, we provide an example comparison between the beta estimates obtained using the bCF_A and the bCF_B models (Supplementary Figure S1 and Figure S2).

3.2. Results of new Bayesian CF functionality

3.2.1. Uncertainty

An important theoretical advantage of the Bayesian approach is that, besides the optimal values of the CF parameters (σ , β , VE), it also determines their associated (posterior) uncertainty.

For illustrative purposes only, Fig. 5 shows the cortical projections of CF size and beta as well as their associated uncertainties for V1>V2 for two participants. In the supplementary materials, cortical projections of eccentricity and polar angle can be found for these two participants (Fig. S6) and further, we show the uncertainty estimates of these same

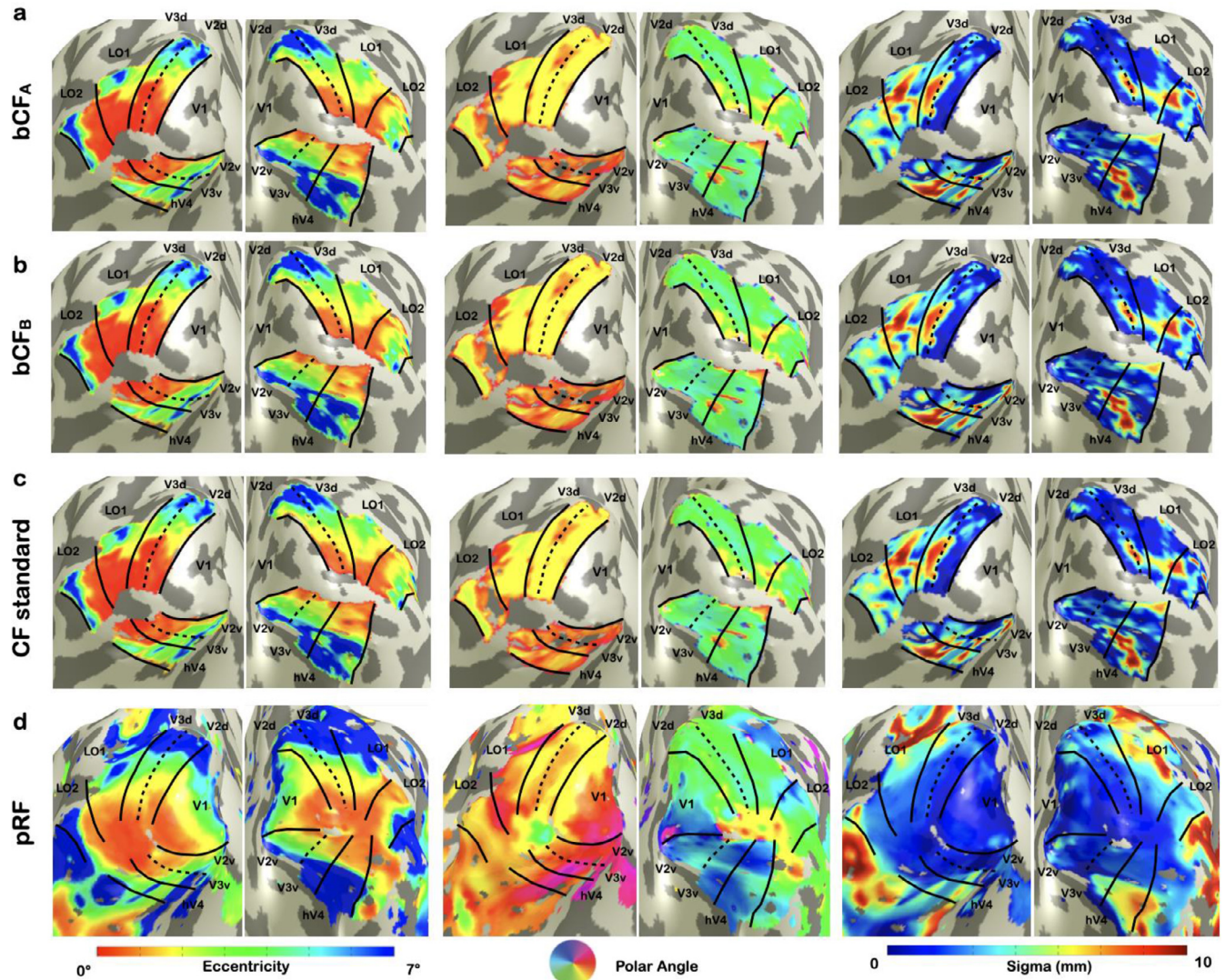


Fig. 3. The Bayesian CF reproduces the basic parameters of the standard CF approach. Panels a and b: maps for eccentricity, polar angle and CF size based on bCF_A and bCF_B, respectively. Panel c: reference maps for eccentricity, polar angle and CF size based on sCF. The left (eccentricity) and middle (polar angle) panels of row a, b and c show retinotopic maps reconstructed via the CF models, using V1 as the source (which is why V1 is absent in these maps). Row d: reference maps for eccentricity, polar angle and pRF size based on population receptive field (pRF)-based retinotopic mapping. For illustrative purposes, the borders between visual areas are indicated by black lines. The ROI definitions used in the analysis are reported in the supplementary material (Fig. S5). The maps are all for a single participant (#2). Fig. 4 shows the voxel level correlations between the sCF and bCF results of this participant.

two participants and for all participants as a function of (pRF-derived) eccentricity (Fig. S7).

Fig. 6 shows the cross-correlation coefficients between the MCMC parameters, the corresponding (posterior) uncertainties and the residual noise. For all target ROIs, VE and the uncertainties for σ and β are moderately and negatively correlated. The bCF parameters are only weakly correlated with their corresponding uncertainties.

3.2.2. Beta thresholding

The bCF_B enables to test whether or not the activity of a voxel in the target region is meaningfully associated to that in the source region, based on the distribution of beta (see Section 2.6.2). For illustration purposes, Fig. 7 shows the distribution of β values estimated for a single V2 target voxel based on either its real (panel 7a) or a surrogate (panel 7b) time-series. The dotted line in panel 7a indicates the optimal estimate. Panel 7c shows the histogram of the best fitting beta obtained using 40 surrogate times series for this voxel. Based on the 95th percentile of the beta distribution over surrogates, a beta-uncorrected threshold can be

defined for this voxel. Panel 7d shows 10 examples of null distributions of beta aggregated over all V2 voxels (each distribution is shown at a different gray level). It is clear that these aggregate distributions are highly comparable and will also result in very similar FWE-corrected beta thresholds.

To evaluate the FWE-corrected beta thresholding method in the voxel selection on VFM data, we compared it to the model VE (Fig. 8). Both thresholds are indicated (panel a): VE higher than 15% and the FWE corrected effect size ($>95\%$). We chose this commonly used, yet arbitrary, VE threshold, while noting that it is substantially less conservative than the 95% FWE beta-threshold. This latter threshold was then used to perform the model comparison.

3.4. Model comparison

In principle, the bCF also enables model comparisons at the voxel level that take the number of free parameters into account. Here, we use the likelihood estimations of the bCF_B (see Section 2.5) to calculate

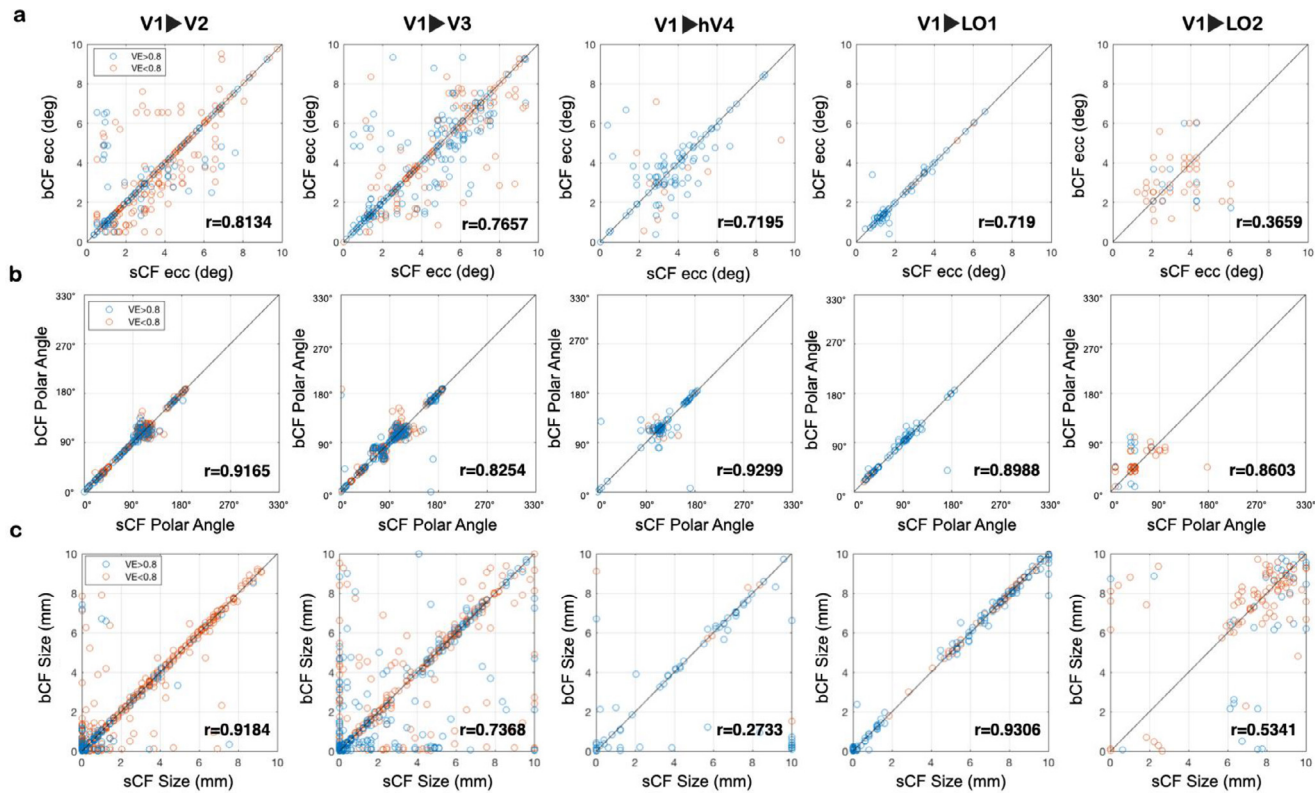


Fig. 4. Voxel level correlations between the results of the standard CF and Bayesian CF. Results are for participant #2, also shown in Fig. 3. Columns from left to right show the CF estimates for the target regions V2, V3, hV4, LO1 and LO2, each of them sampling from source region V1. Panels a, b and c show the (Pearson) correlations for eccentricity and polar angle (both converted into visual field coordinates) and CF size, respectively. Only voxels with a VE > 0.15 for the sCF model fit were considered. Voxel data points are color coded based on their VE: orange indicates a VE in the range 0.15-0.8 while blue indicates a VE higher than 0.8. The voxel level correlation plots for all other participants are reported in supplementary Fig. S4. The correlation values for all participants are reported in the Supplementary Materials (Table T2).

Bayesian Information Criterion (BIC) and Akaike's Information Criterion (AIC) scores and compare whether SG or DoG models better explain the responses of the target voxels. For both criteria, lower values indicate more evidence for a particular model. Fig. 9, panels b and c show that on average, in all visual areas, the voxels have only slightly lower BIC and AIC scores for the SG compared to the DoG. Panels 9d and 9e show that when plotted in terms of their preferred model, the voxels of all areas predominantly prefer the SG model. For comparison, we also compare the fits of the SG and DoG models using VE (Fig. 9a). A slightly higher VE is found for the DoG compared to the SG model across all visual areas but these differences are not significant (p -values range from 0.64 to 0.28 based on 5000 permutations). Furthermore, the BIC values and the difference between the BIC scores of the SG and DoG models at voxels level were projected onto the smoothed cortical surface. No clear visuotopic organization seems to be present (Fig. 9, panels f-h). Additional BIC maps can be found in the Supplementary Materials (Fig. S3).

4. Discussion

In the present work, we show how a Bayesian variant of the CF modeling approach can be used for a detailed assessment of the cortico-cortical properties of the visual system. Importantly, the parameter estimates of the bCF agree with those of the sCF while additionally providing the uncertainties associated with the voxel-level estimates of CF size and effect size (β). Finally, we find that for the majority of voxels in the early visual cortex, a SG is preferred over a DoG model. This suggests that CFs do not possess a center-surround organization. Below, we discuss our results in more detail.

4.1. The Bayesian inference approach accurately characterizes cortico-cortical receptive field properties

We find that the Bayesian Connective Field output compares well to that of the standard approach.

The visuotopic maps based on the bCF are qualitatively similar to those based on the sCF (Fig. 3). When quantified, we found the highest degree of similarity between bCF and sCF for V1 projecting to V2 (V1>V2) and V1 projecting to V3 (V1>V3). Still, substantial inter-subject variability can be observed (e.g., compare Participant #2 shown in Fig. 4 to Participant #6 shown in Fig. S4). Some of this variability may be due to the probabilistic nature of the MCMC procedure. These quantitative and qualitative results are in agreement with those presented previously (Haak et al., 2013). This correspondence indicates that the Bayesian inference approach provides the same parameter estimates while providing new information: the underlying posterior distributions and the uncertainty associated with each parameter.

In the past years, Bayesian approaches have been applied to the pRF method allowing estimation of the full posterior distribution associated with each of the receptive field properties (Zeidman et al., 2018; Quax et al., n.d.; Adaszewski et al., 2018; Benson and Winawer, 2018; Carvalho et al., 2020). Similar to these Bayesian pRF methods, the Bayesian CF framework now provides the full posterior distribution associated with each of the cortico-cortical model parameters. From this, parameter uncertainty can be derived and possible dependencies between parameter estimates can be quantified. Importantly, we find that the uncertainty estimates do not correlate with the parameter estimates themselves (see Fig. 6). At most weak correlations were observed between the bCF parameters and their corresponding uncertain-

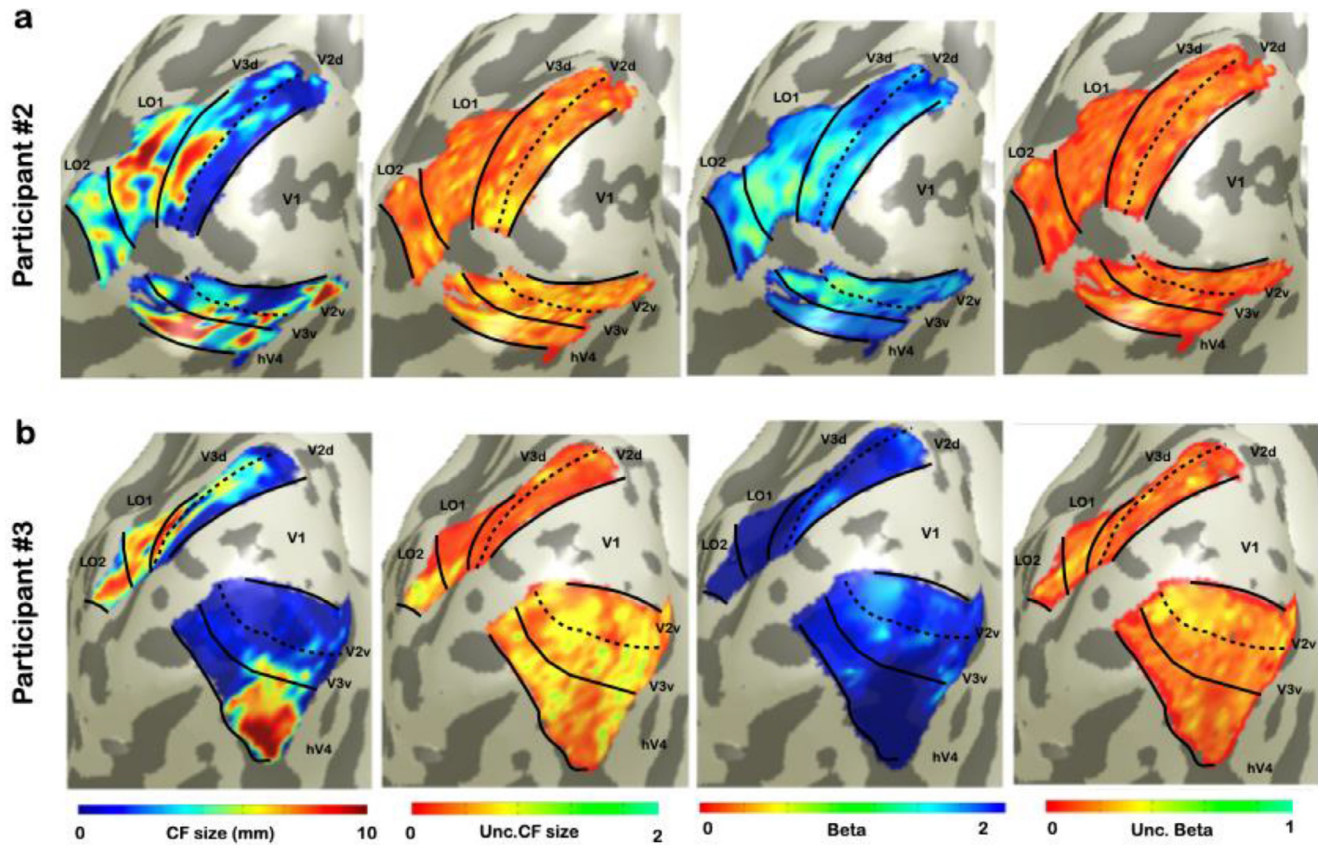


Fig. 5. Illustrative visualization of CF size and beta and their associated uncertainties as estimated using bCF_b for two participants. From left to right: CF size, uncertainty of CF size, beta and uncertainty of beta. Panel a and b show these bCF parameters obtained for participants #2 and #3, respectively. For further illustration, Fig. S7 plots the uncertainties in the CF size and beta for $V1 > V2$ for these two participants (as well as all other participants) as a function of eccentricity. For illustrative purposes, the borders between visual areas are indicated by black lines. The ROI definitions used for analysis are reported in supplementary material (Fig. S5)

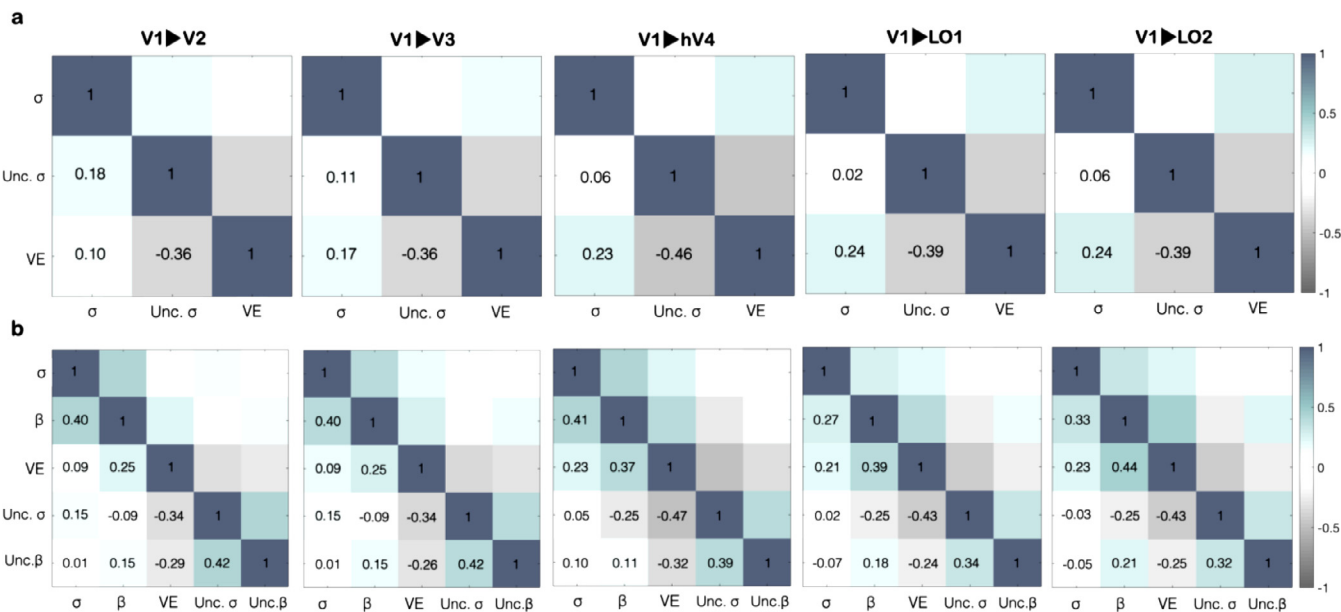


Fig. 6. Cross correlations between bCF parameters and their associated uncertainties at the voxel level. Panels a and b show the correlations obtained using $bCFA$ and $bCFB$, respectively. Only the CF parameters directly estimated using the model (σ, β and VE) are included in this analysis. The bCF parameter values and their associated uncertainties were first estimated at the participant level and then concatenated across all participants to determine the medians. Boxplots of the statistical dependencies between the bCF parameters and their uncertainties are shown in supplementary Fig. S2.

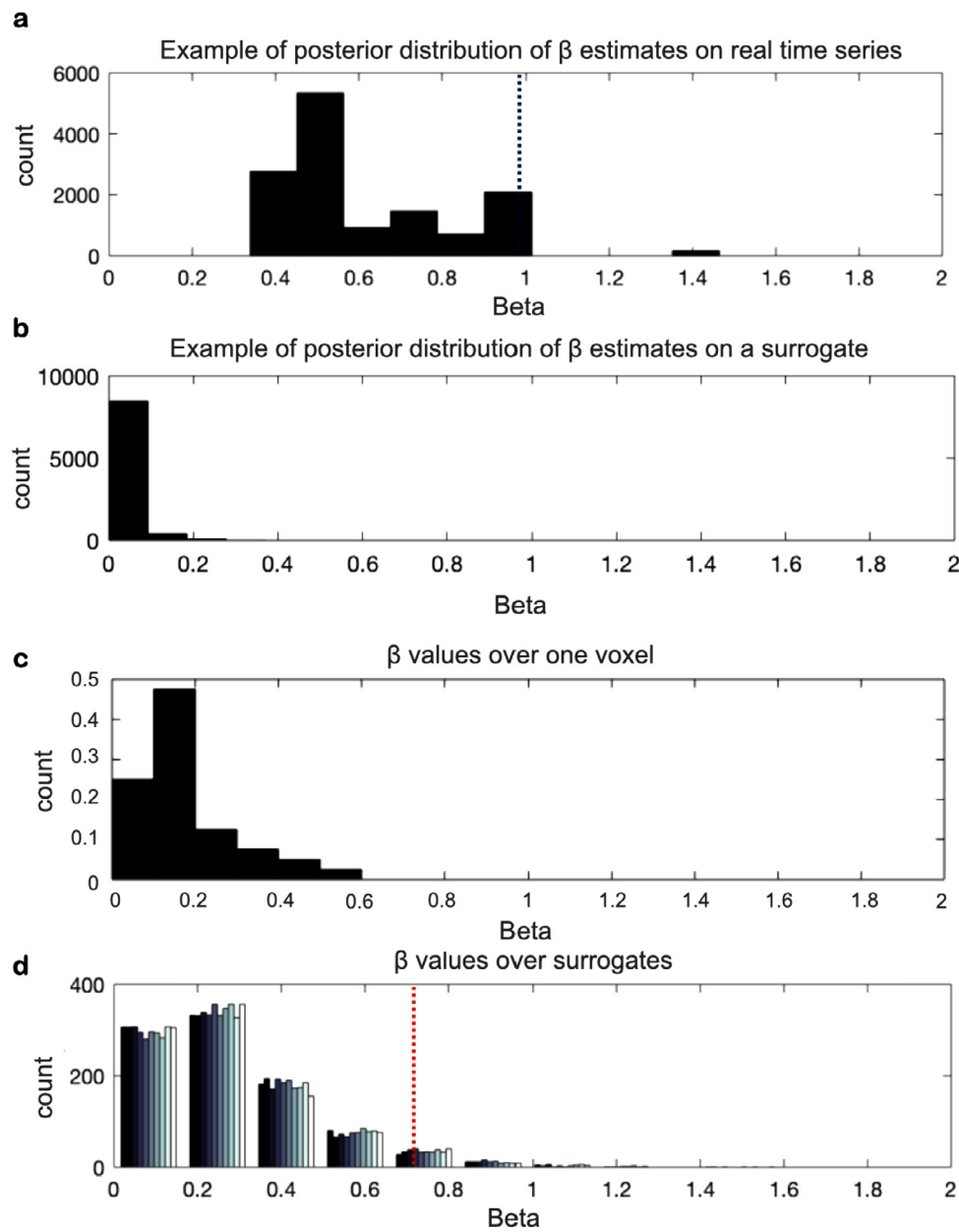


Fig. 7. Illustration of the beta-based threshold distributions and estimates. In panels a and b, the histograms show the posterior distribution of beta for a single target voxel in area V2 (sampling from V1) for a real and surrogate time series, respectively. In panel a, the best fitting bCF beta estimate for this voxel ($\beta = 0.98$) is indicated by the black dotted line. Panel c shows the histogram of the best fitting beta over one voxel. This histogram can be used to obtain an uncorrected threshold. Finally, in panel d, each gray bar shows the distribution of best fitting beta values under the null hypothesis (i.e. surrogate data) across all voxels in V2. Each bar represents a distribution based on one surrogate. For comparison purposes only, we present 10 aggregate distributions. The red dotted line indicates the FWE-corrected beta threshold ($\beta = 0.72$) for one (randomly selected) distribution. A comparison of the beta estimates for both bCF options is reported in supplementary Figs. S1 and S2.

ties (with correlations mostly below 0.25). Therefore, the uncertainty can be treated as an additional, independent CF parameter to quantify reliability. A moderately strong inverse relationship was observed between the goodness of fit of the model (VE) and the uncertainties. While this might suggest the uncertainties do not provide additional information on the data, in the next section we will show they do, nevertheless. The uncertainty may be used in various ways to increase confidence in the CF model predictions. For example, it may be used for statistical comparisons at the level of single individuals, which can be important in the context of patient studies, in particular when assessing rare cases, where group averages are not available. Moreover in patient studies, it will help to quantify the reliability of the estimates in each patient. As we will discuss later, it can also be used to test different models at the single voxel level.

4.2. The effect size provides a data driven threshold

The standard and widely used approach to select the most reliable voxels uses thresholding based on the goodness of fit of the CF model (i.e. on VE; Haak et al., 2013; Halbertsma et al., 2019). However, a high

VE does not necessarily correspond to a low variability in the estimates (Thielen et al., n.d.). In fact, a model fitted to noisy data may still get a high VE. Based on the Bayes CF framework, we developed two thresholding techniques based on the posterior distributions of effect size β : 1) an uncorrected threshold per voxel and 2) a threshold, FWE corrected for all voxels in a target ROI.

It is important to realize that the two model parameters VE and effect size are related but not equivalent. They correspond to different aspects of the model. Consequently, also thresholding based on either of the two parameters will not provide identical effects. VE thresholding is based on the residuals (noise), whereas the effect size is based on the explanatory variables in the model (signal). This means that effect size thresholding can, in principle, still detect a meaningful effect when the target voxel's data is mixed with unmodeled signals. For example, besides the signals from the source region, there likely are other brain areas that cause variance in the target voxel. Their influence is not modeled and will inflate the noise term and lower the VE. Therefore, the VE can be rather low (depending on how the target voxel is embedded in the network) while connection (beta-value) between source region and target voxel is stable and its null hypothesis can be rejected. Fig. 8 illustrates that there are

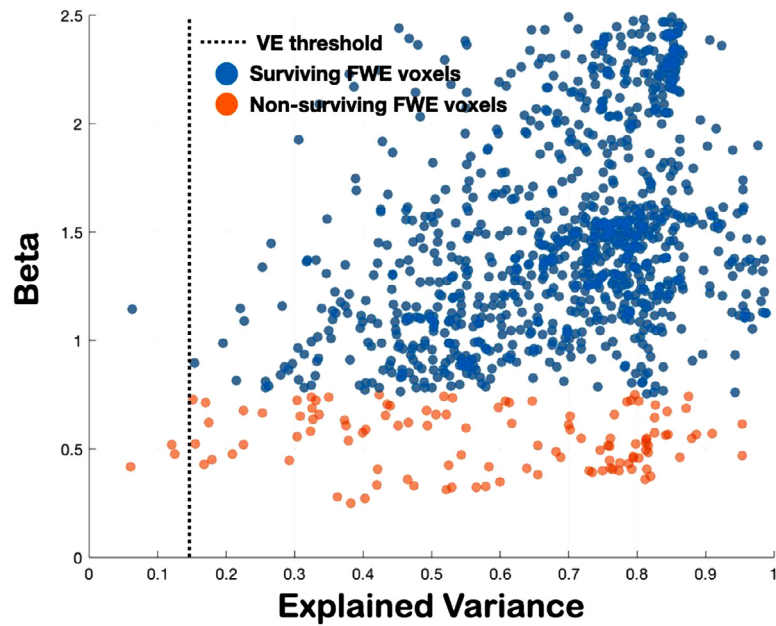


Fig. 8. Comparison of thresholding approaches for one single participant for V1>V2 (right hemisphere) connectivity based on VFM data. The relation between VE and the beta parameter is presented for the voxels surviving the 95% FWE beta-threshold (blue dots) and those not surviving (orange dots) for one single participant for V1>V2 in the right hemisphere. The commonly used, yet arbitrary, VE threshold of 0.15 is indicated by the vertical, black dotted, line.

voxels (in V2) with a relatively low VE and high beta-value (and vice versa). It also shows that there are no threshold values for beta and VE that would provide equivalent thresholding. The suitability and gain of the new threshold options depends on the goals of a study. We expect that the *beta*-thresholds will be particularly useful when bCF modeling is applied in clinical populations (e.g. with a lesioned visual pathway or cortical neurodegeneration). Deriving these *beta*-thresholds requires the generation of a proxy distribution for the null hypothesis based on surrogate BOLD time series. At present, obtaining voxel-specific thresholds is computationally demanding or time consuming. This is less so for the FWE corrected threshold where a single surrogate BOLD time series per voxel will suffice. We verified this by generating 40 surrogate null-distributions across the voxels of an area which turned out to be highly consistent (see Fig. 7d). Finally, note that the beta-value thresholds are data-driven and thus participant- and even area- or voxel-specific.

4.3. Comparing different models for Connective Fields

Another functionality gained through the bCF is the ability to compare different cortical receptive field models at the voxel level. In pRF modelling, a larger VE was reported for a Difference of Gaussian (DoG) pRF model compared to a single Gaussian (SG) model in the early visual cortical areas (Zuiderbaan et al., 2012; Zeidman et al., 2018). Therefore, a DoG pRF model may better explain the observed fMRI signal in the early visual cortex. Moreover, being able to assess this feature is useful, as center-surround configurations of pRFs may be different in clinical populations (Anderson et al., 2017; Zhang et al., 2009; Grigorescu et al., 2003).

To illustrate the new bCF functionality, we compared a SG CF model to a DoG CF model on the basis of VE, AIC and BIC values. On average, a slightly larger but non-significant difference in VE was observed for the DoG compared to the SG CF models in all the visual cortical areas (see Figs. 9; S3). However, *a priori* a higher VE for the DoG is expected due to its additional degrees of freedom (4 rather than 2 for the SG; Haefner and Cumming, 2008; Singh and Horn, 1999). In contrast, the model complexity is taken into account by AIC and BIC scores. On average, the differences between the SG and DoG model using AIC and BIC scores were very small. Nevertheless, on the basis of either score, the majority of the voxels (~ 80%) in all visual areas seems to prefer the SG model at cortical level. This indicates that the more complex DoG CF model may overfit the data.

4.4. Limitations

In analogy to the standard CF model, we forced the CF center (i.e. the center of the gaussian kernel) to coincide with a vertex in the source region. In the MCMC procedure, the distance of the accepted CF center to other voxels is computed using Dijkstra's algorithm (Dijkstra, 1959); as implemented in the mrVista environment. Thus, the CF location/center is discrete since distance is based on the vertices of a mesh. In addition, forcing the CF center to coincide with a vertex may induce an 'edge effect' as the model cannot sample outside of the source region. In particular, near the edges of the source region this may influence the symmetry in the chosen step updates which, in turn, may cause an asymmetry bias in the sampled locations. Note, however, that we did not observe such an effect in our visual field reconstruction. Although location sampling may be biased near the edges, this will have only minimal impact on our results as we only use the "optimal-fit location" for further analysis.

Compared to the sCF, the bCF framework is computationally demanding. Currently, we addressed this by using parallel GPU computing and implementing the method using cluster computing (<https://wiki.hpc.rug.nl/peregrine/start>) - per node, we used 48 Intel Xeon 2.5 GHz cores with 512 GB of internal memory (Avesani et al., 2019). We employed 17500 iterations and removed the initial 10% to account for bleed in. This provided a decent sampling of the posterior distribution in a reasonable amount of time (~ 21h per visual area). It is possible that increasing the number of iterations may improve the posterior distribution estimate. This was not explored further in this paper. Future advances in hardware, software and code optimization (i.e. code can be rewritten in a more performant language, like JIT, Python or C, for substantially better performance) will contribute to reducing the computation time. Furthermore, a thinning procedure to reduce the memory demand may be considered.

Thus far, when comparing models, possible autocorrelations in the time courses of the source region, as well as possible covariations between parameter estimates during the MCMC iteration process have not been accounted for. The first point may result in an overestimation of the effective number of points (degree of freedom) which will impose an additional penalty when adding parameters to the model. The second point may overestimate the number of independent/free parameters, again posing a (possible) additional penalty on increasing the number of parameters. Taken together, the model comparison that we have performed thus far, is bound to be conservative, i.e. it will tend to favour the model with fewer parameters. Finally, although simulations indicate

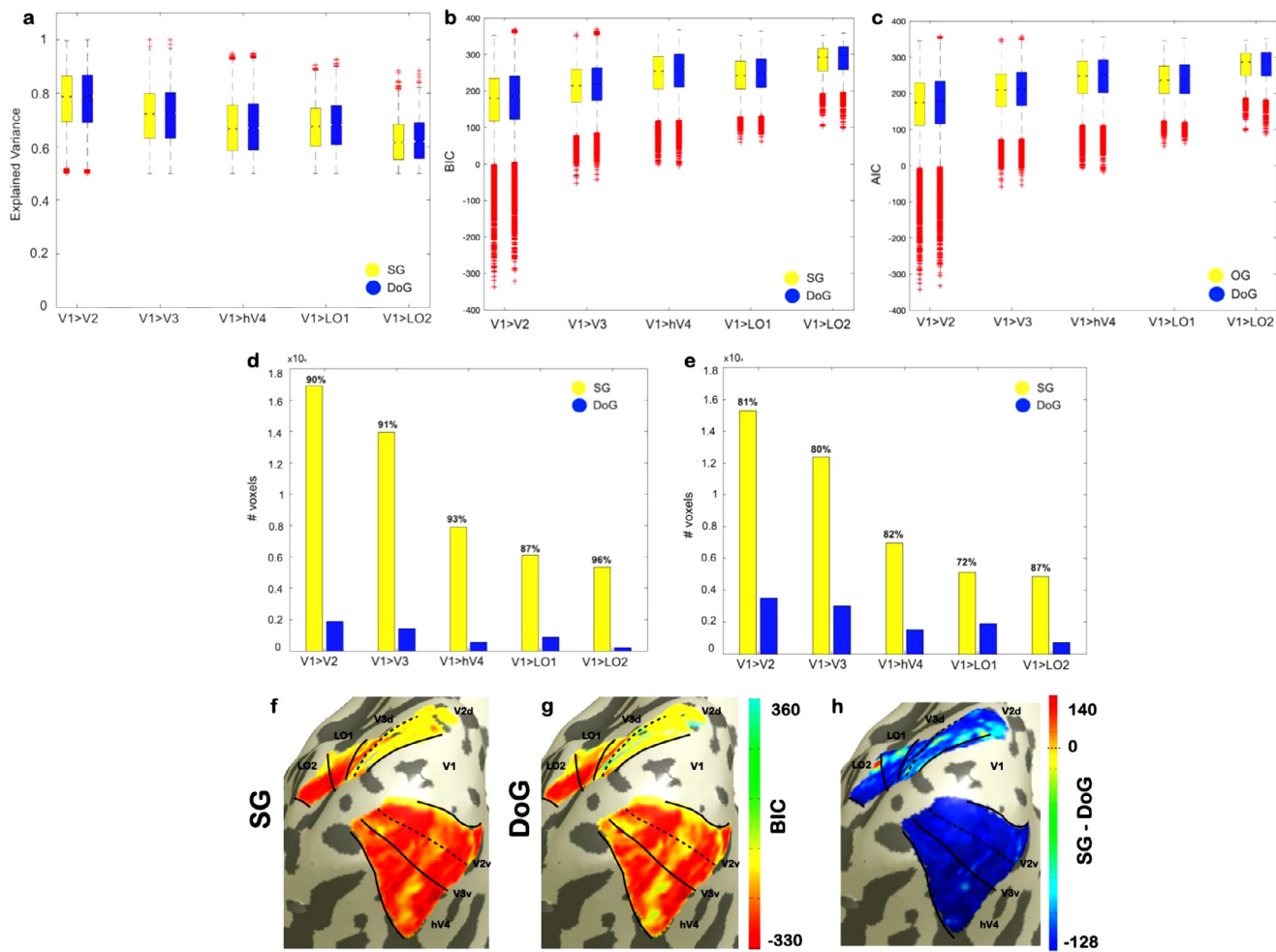


Fig. 9. Model comparison between SG and DoG bCF models. Variance explained and BIC were computed at the single subject level and then averaged over the population per ROI for both the SG and DoG bCF models. Data was thresholded using the confidence interval (CI) corrected beta-based option. Panels a,b and c show for both models the Explained Variance, BIC and AIC scores, respectively. For almost all ROIs, the DoG CF model (blue) has a larger VE compared to SG CF model (yellow). Note that red crosses indicate data that are outside the 25th-75th percentile. Panels d and e show per ROI the number of voxels with a lower BIC or lower AIC, respectively. The percentage is provided on top of each bar for the SG model. In all ROIs, the simpler model is favored when the number of model parameters is taken into account. Panels f and g show, for a single participant (#3), the projections of the BIC values onto a smoothed cortical surface for the SG and DoG CF models, respectively. Panel h shows, for the same participant, the projections of the BIC difference between two CF models (SG - DoG), with more negative values indicating greater evidence for the SG model. For illustrative purposes, borders between visual areas are indicated by black lines. The ROI definitions used for analysis are reported in supplementary Fig. S5.

that the current implementation can in principle distinguish models (see supplementary materials S4), it is possible that the current implementation (i.e. modeling assumptions) is not optimally sensitive to subtle model differences (as suggested by the limited differences in VE, BIC and AIC estimates in Fig. 9).

4.5. Future directions

The bCF presented here uses a straightforward biological-grounded model to assess the cortical receptive field properties, and provides a starting point for future studies.

Similar to the sCF model, the bCF model is stimulus-agnostic. Previous studies have shown that the sCF still reflects the visuotopic organization of the visual cortex when applied to BOLD activity recorded in the absence of external stimulation (i.e. resting-state fMRI data; (Gravel et al., 2014; Bock et al., 2015)). In a similar way, the bCF model will be able to extract connectivity based on intrinsic activity. Thus, it may be used to evaluate the quality of cortical processing in participants in which the visual input may be compromised by ocular or neurological lesions (Carvalho et al., 2019).

The bCF may allow better monitoring of disease progression or the effect of an intervention. Beta and the associated uncertainty can be used to rate data and model fit quality in individual participants. Moreover, the uncertainty associated with other parameters can be used to weight the contribution of a participant to a group average. This may improve our insights into the cortical components of neurological or neuro-ophthalmic diseases, such as e.g. glaucoma or Parkinson's disease.

Future implementations of the code should incorporate methods to account for (possible) autocorrelations in the time series of the source, as well as covarying parameter estimates during the MCMC iteration process. For example, the first issue may be ameliorated by implementing a “thinning” procedure, whereas the covariance between parameters can be estimated from the MCMC iterations. This may provide further insight in the interdependencies introduced by the model which may affect efficient estimation.

Our bCF framework allows comparison of different models to represent the CF which may provide novel information on how cortical regions exactly interact as well as help characterize changes in cortical mechanisms in neuro-ophthalmic patients. Besides the DoG model,

the bCF may be used to test further model definitions that may characterize properties of the cortical interactions between visual areas (i.e. uniform or square shape, elongated shape, oriented ellipse, polar Gaussian, Cartesian and Polar Log-Gaussian, or divisive normalization (Kumano and Uka, 2010; Zeidman et al., 2018; Aqil et al., 2021). Notably, the bCF framework enables proper cortical model comparison by estimating the likelihood of a model. This allows to implement further Bayesian model selection using various criteria such as Bayes Factor or Free Energy (Penny 2012; Edwards et al., 2010). By estimating and selecting at the voxel level, such criteria or properties may be projected onto the cortical surface (or other representations) to investigate their possible visuotopic (re-)organization.

5. Conclusion

In this study, we have presented and validated a Bayesian inference framework for CF modeling that is based on a Markov Chain Monte Carlo approach. When applied to empirical stimulus-driven fMRI data, we observed good agreement of the bCF and the sCF outputs.

The bCF approach has enabled various new functionalities. First, it quantifies the parameter uncertainty associated with the CF parameters which may be used in various ways to increase confidence in the parameter estimates. Second, the effect size of the BOLD fluctuation (beta) can now be used to derive a reliable, data-driven threshold. Third, it enables voxel level comparison of different CF kernels. We conclude that our Bayesian CF framework provides a versatile tool to study the properties of the cortical interactive processes underlying perception, attention and cognition in health, development, aging and disease.

Funding

AI and JC were supported by the European Union's Horizon 2020 research and innovation programme under the Marie Skłodowska-Curie grant agreement No. [661883](#) (EGRET) and No. [641805](#) (NextGenVis). AI and JC received additional funding from the Graduate School of Medical Sciences (GSMS), University of Groningen, The Netherlands. KVH gratefully acknowledges funding from the Netherlands Organisation for Scientific Research (NWO Veni grant no. 016.Veni.171.068 and Vidi grant no. [09150171910043](#)). The funding organizations had no role in the design, conduct, analysis, or publication of this research.

Data and Code Availability Statement

Raw and derived data that support the findings of this study are available from the corresponding author, Azzurra Invernizzi, upon reasonable request.

The code presented in this manuscript will be made openly available after acceptance at <http://www.visualneuroscience.nl>

Sincerely yours, on the behalf of all authors, Azzurra Invernizzi, PhD

Data Availability

Data will be made available on request.

Acknowledgements

We want to thank Hinke N. Halbertsma for data collection and pRF data analysis.

Supplementary materials

Supplementary material associated with this article can be found, in the online version, at doi:[10.1016/j.neuroimage.2022.119688](https://doi.org/10.1016/j.neuroimage.2022.119688).

References

- Adaszewski, S., Slater, D., Melie-Garcia, L., Draganski, B., Bogorodzki, P., 2018. Simultaneous estimation of population receptive field and hemodynamic parameters from single point BOLD responses using metropolis-hastings sampling. Neuroimage 172 (May), 175–193.
- Ahmadi, K., Herbig, A., Wagner, M., Kanowski, M., Thieme, H., Hoffmann, MB., 2019. Population receptive field and connectivity properties of the early visual cortex in human albinism. Neuroimage 202 (November), 116105.
- Amano, K., Wandell, BA., Dumoulin, SO., 2009. Visual field maps, population receptive field sizes, and visual field coverage in the human MT+ complex. J. Neurophysiol. 102 (5), 2704–2718.
- Anderson, E.J., Tibber, M.S., Sam Schwarzkopf, D., Shergill, S.S., Fernandez-Egea, E., Rees, G., Dakin, S.C., 2017. Visual Population receptive fields in people with Schizophrenia have reduced inhibitory surrounds. J. Neurosci. 37 (6), 1546–1556.
- Aqil, M., Knapen, T., Dumoulin, SO., 2021. Divisive normalization unifies disparate response signatures throughout the human visual hierarchy. Proc. Nat. Acad. Sci. U.S.A. 118 (46). doi:[10.1073/pnas.2108713118](https://doi.org/10.1073/pnas.2108713118).
- Avesani, P., McPherson, B., Hayashi, S., Caiafa, C.F., Henschel, R., Garyfallidis, E., Kitchell, L., et al., 2019. The open diffusion data derivatives, brain data upcycling via integrated publishing of derivatives and reproducible open cloud services. Sci. Data 6 (1), 69.
- Baseler, H.A., Gouws, A., Haak, K.V., Racey, C., Crossland, M.D., Tufail, A., Rubin, G.S., Cornelissen, F.W., Morland, A.B., 2011. Large-scale remapping of visual cortex is absent in adult humans with macular degeneration. Nat. Neurosci. 14 (5), 649–655.
- Benson, N.C., Winawer, J., 2018. Bayesian analysis of retinotopic maps. Elife (December) 7. doi:[10.7554/elife.40224](https://doi.org/10.7554/elife.40224).
- Bock, A.S., Binda, P., Benson, N.C., Bridge, H., Watkins, K.E., Fine, I., 2015. Resting-state retinotopic organization in the absence of retinal input and visual experience. J. Neurosci. 35 (36), 12366–12382.
- Brainard, D.H., 1997. The psychophysics toolbox. Spat. Vis. 10 (4), 433–436.
- Brewer, A.A., Liu, J., Wade, A.R., Wandell, B.A., 2005. Visual field maps and stimulus selectivity in human ventral occipital cortex. Nat. Neurosci. 8 (8), 1102–1109.
- Wandell, B.A., Winawer, J., 2011. Imaging retinotopic maps in the human brain. Vision Res. 51 (7), 718.
- Carvalho, J., Invernizzi, A., Ahmadi, K., Hoffmann, M.B., Renken, R.J., Cornelissen, F.W., 2020. Micro-probing enables fine-grained mapping of neuronal populations using fMRI. Neuroimage 209 (April), 116423.
- Carvalho, J., Renken, R.J., Cornelissen, F.W., 2019. Studying cortical plasticity in ophthalmic and neurological disorders: from stimulus-driven to cortical circuitry modeling approaches. Neural Plast. 2019 (November), 2724101.
- Chib, S., 2011. Introduction to simulation and MCMC methods. Oxf. Handb. Bayesian Econ. doi:[10.1093/oxfordhb/9780199559084.013.0006](https://doi.org/10.1093/oxfordhb/9780199559084.013.0006).
- De Best, P.B., Raz, N., Guy, N., Ben-Hur, T., Dumoulin, S.O., Pertzov, Y., Levin, N., 2019. Role of population receptive field size in complex visual dysfunctions: a posterior cortical atrophy model. JAMA Neurol. 76 (11), 1391–1396.
- Dijkstra, E.W., 1959. A note on two problems in connexion with graphs. Numer. Math. doi:[10.1007/bf01386390](https://doi.org/10.1007/bf01386390).
- Dougherty, R.F., Koch, V.M., Brewer, A.A., Fischer, B., Modersitzki, J., Wandell, B.A., 2003. Visual field representations and locations of visual areas V1/2/3 in human visual cortex. J. Vis. 3 (10), 1. doi:[10.1167/3.10.1](https://doi.org/10.1167/3.10.1).
- Dumoulin, S.O., Wandell, B.A., 2008. Population receptive field estimates in human visual cortex. Neuroimage 39 (2), 647–660.
- Edwards, D., Gabriel, C.G., de, A., Labouriau, R., 2010. Selecting high-dimensional mixed graphical models using minimal AIC or BIC forests. BMC Bioinf. doi:[10.1186/1471-2105-11-18](https://doi.org/10.1186/1471-2105-11-18).
- Engel, S.A., Glover, G.H., Wandell, B.A., 1997. Retinotopic organization in human visual cortex and the spatial precision of functional MRI. Cereb. Cortex 7 (2), 181–192.
- “FSL”, 2012. Neuroimage 62 (2), 782–790.
- Gravel, N., Harvey, B., Nordhjem, B., Haak, K.V., Dumoulin, S.O., Renken, R., Curcić-Blake, B., Cornelissen, F.W., 2014. Cortical connective field estimates from resting state fMRI activity. Front. Neurosci. 8 (October), 339.
- Grigorescu, C., Petkov, N., Westenberg, M.A., 2003. Contour detection based on nonclassical receptive field inhibition. IEEE Trans. Image Process. 12 (7), 729–739.
- Haak, K.V., Cornelissen, F.W., Morland, A.B., 2012. Population receptive field dynamics in human visual cortex. PLoS One 7 (5), e37686.
- Haak, K.V., Morland, A.B., Rubin, G.S., Cornelissen, F.W., 2016. Preserved retinotopic brain connectivity in macular degeneration. Ophthalmic Physiol. Opt. 36 (3), 335–343.
- Haak, K.V., Winawer, J., Harvey, B.M., Renken, R., Dumoulin, S.O., Wandell, B.A., Cornelissen, F.W., 2013. Connective field modeling. Neuroimage 66 (February), 376–384.
- Haak, K.V., Morland, A.B., Cornelissen, F.W., 2013. Connective field estimates in the cortical lesion project zone of individuals with macular degeneration. J. Vis. doi:[10.1167/13.15.11](https://doi.org/10.1167/13.15.11).
- Halbertsma, H.N., Haak, K.V., Cornelissen, F.W., 2019. Stimulus- and neural-referred visual receptive field properties following hemispherectomy: a case study revisited. Neural Plast. 2019 (September), 6067871.
- Harvey, B.M., Dumoulin, S.O., 2011. The relationship between cortical magnification factor and population receptive field size in human visual cortex: constancies in cortical architecture. J. Neurosci. 31 (38), 13604–13612.
- Invernizzi, A., Gravel, N., Haak, K.V., Renken, R.J., Cornelissen, F.W., 2021. Assessing uncertainty and reliability of connective field estimations from resting state fMRI activity at 3T. Front. Neurosci. doi:[10.3389/fnins.2021.625309](https://doi.org/10.3389/fnins.2021.625309).
- Kumano, H., Uka, T., 2010. The spatial profile of macaque MT neurons is consistent with gaussian sampling of logarithmically coordinated visual representation. J. Neurophysiol. 104 (1), 61–75.

- Liu, J., Nordman, D.J., Meeker, W.Q., 2016. The number of MCMC draws needed to compute bayesian credible bounds. *Am. Stat.* doi:[10.1080/00031305.2016.1158738](https://doi.org/10.1080/00031305.2016.1158738).
- Meindertsma, T., Kloosterman, N.A., Nolte, G., Engel, A.K., Donner, T.H., 2017. Multiple transient signals in human visual cortex associated with an elementary decision. *J. Neurosci.* 37 (23), 5744–5757.
- Myung, J.I., Pitt, M.A., 2004. Model comparison methods. *Methods Enzymol.* doi:[10.1016/s0076-6879\(04\)83014-3](https://doi.org/10.1016/s0076-6879(04)83014-3).
- Nestares, O., Heeger, D.J., 2000. Robust multiresolution alignment of MRI brain volumes. *Magn. Reson. Med.* 43 (5). doi:[10.1002/\(sici\)1522-2594\(200005\)43:5<705::aid-mrm13>3.0.co;2-r](https://doi.org/10.1002/(sici)1522-2594(200005)43:5<705::aid-mrm13>3.0.co;2-r).
- Papadopoulos, C.E., Yeung, H., 2001. Uncertainty estimation and Monte Carlo simulation method. *Flow Meas. Instrum.* doi:[10.1016/s0955-5986\(01\)00015-2](https://doi.org/10.1016/s0955-5986(01)00015-2).
- Park, S.-J., Shin, J.-K., Lee, M., 2002. Biologically inspired saliency map model for bottom-up visual attention. *Biol. Motivated Comput. Vis.* doi:[10.1007/3-540-36181-2_42](https://doi.org/10.1007/3-540-36181-2_42).
- Pelli, D.G., 1997. The VideoToolbox software for visual psychophysics: transforming numbers into movies. *Spat. Vis.* 10 (4), 437–442.
- Penny, W.D., 2012. Comparing dynamic causal models using AIC, BIC and free energy. *Neuroimage* 59 (1), 319–330.
- Quax, S.C., Koppen, T.C., Jylänki, P., Dumoulin, S.O., and van Gerven, M.A.J.. n.d. “Slice-sampled Bayesian PRF mapping.” <https://doi.org/10.1101/093724>.
- Räth, C., Monetti, R., 2009. Surrogates with random fourier phases. *Top. Chaotic Syst.* doi:[10.1142/9789814271349_0031](https://doi.org/10.1142/9789814271349_0031).
- Robert, C., Casella, G., 2011. A short history of Markov chain Monte Carlo: subjective recollections from incomplete data. *Stat. Sci.* doi:[10.1214/10-sts351](https://doi.org/10.1214/10-sts351).
- Robinson, D.A., 1989. Integrating with neurons. *Annu. Rev. Neurosci.* 12, 33–45.
- Schira, M.M., Tyler, C.W., Breakspear, M., Spehar, B., 2009. The foveal confluence in human visual cortex. *J. Neurosci.* 29 (28), 9050–9058.
- Schreiber, T., Schmitz, A., 1996. Improved surrogate data for nonlinearity tests. *Phys. Rev. Lett.* doi:[10.1103/physrevlett.77.635](https://doi.org/10.1103/physrevlett.77.635).
- Schwarz, G., 1978. Estimating the dimension of a model. *Ann. Stat.* doi:[10.1214/aos/1176344136](https://doi.org/10.1214/aos/1176344136).
- Sereno, M.I., McDonald, C.T., Allman, J.M., 1994. Analysis of retinotopic maps in extrastriate cortex. *Cereb. Cortex* doi:[10.1093/cercor/4.6.601](https://doi.org/10.1093/cercor/4.6.601).
- Smith, S.M., Jenkinson, M., Woolrich, M.W., Beckmann, C.F., Behrens, T.E., Johansen-Berg, H., Bannister, P.R., et al., 2004. Advances in functional and structural MR image analysis and implementation as FSL. *Neuroimage* 23. doi:[10.1016/j.neuroimage.2004.07.051](https://doi.org/10.1016/j.neuroimage.2004.07.051), Suppl 1.
- Thielen, J., Güçlü, U., Güçlütürk, Y., Ambrogioni, L., Bosch, S.E., and van Gerven, M.A.J.. n.d. “DeepRF: ultrafast population receptive field mapping with deep learning.” doi:[10.1101/732990](https://doi.org/10.1101/732990).
- Wandell, B.A., Dumoulin, S.O., Brewer, A.A., 2007. Visual Field maps in human cortex. *Neuron* 56 (2). doi:[10.1016/j.neuron.2007.10.012](https://doi.org/10.1016/j.neuron.2007.10.012).
- Wandell, B.A., Wade, A.R., 2003. Functional imaging of the visual pathways. *Neurol. Clin.* 21 (2), 417–443 vi.
- Wandell, B.A., Winawer, J., 2015. Computational neuroimaging and population receptive fields. *Trends Cognit. Sci.* 19 (6), 349–357.
- Wang, L., Mruczek, R.E.B., Arcaro, M.J., Kastner, S., 2015. Probabilistic maps of visual topography in human cortex. *Cereb. Cortex* 25 (10), 3911.
- Winawer, J., Horiguchi, H., Sayres, R.A., Amano, K., Wandell, B.A., 2010. Mapping hV4 and ventral occipital cortex: the venous eclipse. *J. Vis.* 10 (5). doi:[10.1167/10.5.1](https://doi.org/10.1167/10.5.1).
- Woolrich, M.W., Jbabdi, S., Patenaude, B., Chappell, M., Makni, S., Behrens, T., Beckmann, C., Jenkinson, M., Smith, S.M., 2009. Bayesian analysis of neuroimaging data in FSL. *Neuroimage* 45 (1). doi:[10.1016/j.neuroimage.2008.10.055](https://doi.org/10.1016/j.neuroimage.2008.10.055), Suppl.
- Zeidman, P., Silson, E.H., Schwarzkopf, D.S., Baker, C.I., Penny, W., 2018. Bayesian population receptive field modelling. *Neuroimage* 180 (Pt A), 173–187.
- Zhang, S., Abbey, C.K., Eckstein, M.P., 2009. Virtual evolution for visual search in natural images results in behavioral receptive fields with inhibitory surrounds. *Vis. Neurosci.* doi:[10.1017/s0952523809090014](https://doi.org/10.1017/s0952523809090014).
- Zuiderbaan, W., Harvey, B.M., Dumoulin, S.O., 2012. Modeling center-surround configurations in population receptive fields using fMRI. *J. Vis.* 12 (3). doi:[10.1167/12.3.10](https://doi.org/10.1167/12.3.10).